Physics Faculty Research

Physics

Winter 1-27-2014

Fracture and Failure of Nanoparticle Monolayers and Multilayers

Yifan Wang

Pongsakorn Kanjanaboos

Edward Barry Edward Barry

Sean P. McBride
Marshall University, mcbrides@marshall.edu

Xiao-Min Lin

See next page for additional authors

Recommended Citation

Wang, Y., Kanjanaboos, P., Barry, E., Mcbride, S., Lin, X. M., & Jaeger, H. M. Fracture and failure of nanoparticle monolayers and multilayers. Nano Lett. 2014. 14(2), 826-830.

Authors

Yifan Wang, Pongsakorn Kanjanaboos, Edward Barry Edward Barry, Sean P. McBride, Xiao-Min Lin, and Heinrich M. Jaeger

Fracture and Failure of Nanoparticle Monolayers and Multilayers

Yifan Wang,*[†,‡] Pongsakorn Kanjanaboos,[†,‡] Edward Barry,[§] Sean Mcbride,[‡] Xiao-Min Lin,[§] and Heinrich M. Jaeger[†,‡]

[†]Department of Physics, University of Chicago, 5720 S. Ellis Avenue, Chicago, Illinois 60637, United States
[‡]James Franck Institute, University of Chicago, 929 E. 57th Street, Chicago, Illinois 60637, United States
[§]Center for Nanoscale Materials, Argonne National Laboratory, 9700 South Cass Avenue, Argonne, Illinois 60439, United States

ABSTRACT: We present an experimental investigation of fracture in self-assembled gold nanoparticle mono- and multilayers attached to elastomer substrates and subjected to tensile stress. Imaging the fracture patterns down to the scale of single particles provides detailed information about the crack width distribution and allows us to compare the scaling of the average crack spacing as a function of strain with predictions by shear-lag models. With increasing particle size, the fracture strength is found to increase while it decreases as the film thickness is built up layer by layer, indicating stress inhomogeneity in the thickness dimension.

KEYWORDS: Self-assembly, nanoparticles, crack, fracture strength, monolayers, multilayers
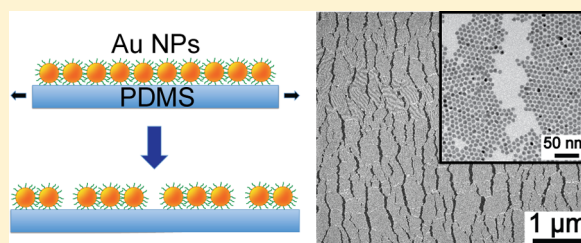
In recent years, much interest has focused on solids configured from ligand-coated nanoparticles, as they combine specific optical, electronic, or magnetic functionality of nanoparticles with the flexibility of self-assembly.[1−6] In these solids, metallic or semiconducting particles, separated by short molecular linkers or ligands, play the role of "designer atoms" that can organize into superlattice configurations.[1,2,6,7] However, for these systems one of the key questions in materials science has remained largely unanswered, namely when and how failure under applied stress loading occurs.[8−12]

Here, we address this for failure under tensile load and focus on the ultrathin film limit in which the thickness approaches that of a single layer of nanoparticles. In this limit, technologically relevant for flexible coatings and self-assembled electronic components, uniform monolayers of close-packed particles with few major defects prior to applying any strain can be fabricated and multilayered structures can be assembled with precision by successively depositing layers one at a time. Given the hybrid organic−inorganic nature of nanoparticle films, intriguing issues include to what extent the linkers can withstand stresses before rupturing and how the fracture patterns differ from those of ultrathin coatings of pure inorganic material. A special feature of nanoparticle monolayers is that, unlike in atomic systems, fracture patterns can be imaged with relative ease down to individual constituent particles using scanning and transmission electron microscopy (SEM and TEM). Statistical analysis of the distribution of crack fragment widths then provides estimates of the intrinsic fracture strength set by the ligand-mediated interparticle bonds.

In our experiments, the nanoparticles consist of gold cores stabilized by dodecanethiol ligands in either toluene or chloroform. Particles with core diameters of 5.2 ± 0.3 nm were synthesized using digestive ripening techniques,[13,14] and particles of 9.1 ± 0.5 nm in diameter were synthesized through citrate reduction in water and subsequently transferred into organic solvents.[15] Nanoparticles were assembled at an air−water interface by adding 30 μL of a concentrated solution to droplets of 18.2 MΩ distilled water (300 μL).[13,16−19] Under these conditions, drying-mediated self-assembly results in close-packed monolayers that are mechanically robust and have Young's moduli E_f on the order of ∼5 GPa.[13,16] The monolayers were transferred onto polydimethylsiloxane (PDMS) substrates (6.0 cm × 1.5 cm × 5 mm) by gently placing the substrate into contact with a monolayer. The PDMS substrates were made by mixing the base and curing agent (SYLGARD 184 Silicone Elastomer Kit, Fisher Scientific) with a ratio of 7:1, followed by degassing and curing at 70 °C for an hour. Atomic force microscopy (AFM) characterization of the PDMS gave a Young's modulus E_s ≈ 2.9 MPa and a rms roughness of <1 nm (measured over 400 μm² as well as 1 μm² areas). With the monolayer attached, the elastomer substrate was stretched in a Instron 5869 materials tester (Figure 1a). A strain rate of ∼0.01 s⁻¹ was used to ensure that the process was quasi-static. At this strain rate, the viscous modulus of our PDMS material, measured directly with a rheometer (MCR 301, Anton Paar), was 0.03 MPa; since this is only about 1% of E_s, viscous effects from the substrate can thus be neglected. Once in their strained state, the Au nanoparticle monolayers were removed from the PDMS and fixed to a solid surface by pressing a clean piece of silicon against them. A FEI Nova NanoLab SEM was used to image the crack pattern. For the data discussed below, 3 independent samples at each strain
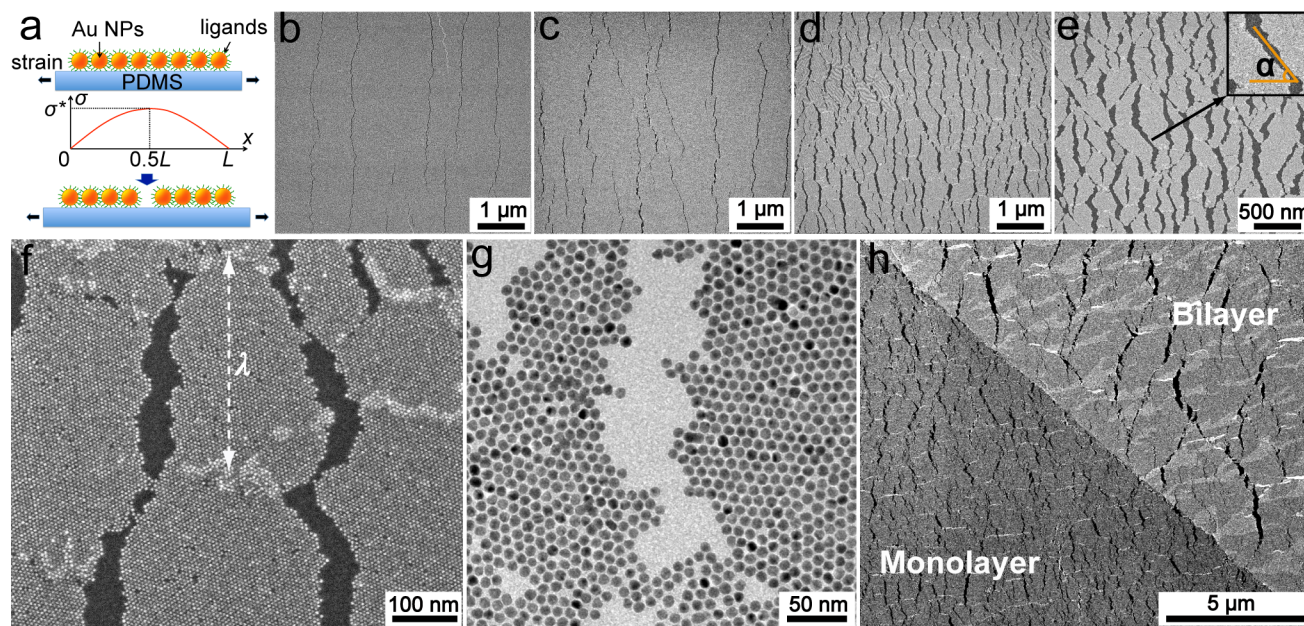
Figure 1. (a) Sketch of Au nanoparticle monolayer on PDMS substrate and crack formation under applied strain. In the shear-lag model, the tensile stress σ is largest in the center of a region of width L. (b−e) Scanning electron microscope (SEM) images of monolayers of 5.2 nm diameter nanoparticles after applying 5, 8, 30, and 60% strain (left to right). Inset to (e) shows zoomed-in image of a crack and definition of crack angle α. (f) Higher-magnification detail of monolayer (d) under 30% strain, dashed line shows wavelength of white strips. (g) Transmission electron microscope (TEM) detail of a 9.1 nm diameter nanoparticle monolayer under 20% strain. (h) SEM image of step-edge region with monolayer in the lower left and bilayer in upper right (9.1 nm diameter Au nanoparticles). The second layer was stamped onto the first layer before the underlying PDMS substrate was strained to 20%. In all images (b−h), the loading direction is horizontal.

level were investigated and for each sample over 20 SEM images, taken at random locations, were analyzed. For the remainder of this discussion, the term "fracture" refers only to fracture of monolayers and multilayers, because fracture of the substrate did not occur for the strain levels applied.

Representative images of the observed crack patterns are shown in Figure 1b−e. We note that the as-deposited monolayers in our experiments were highly uniform on scales beyond a few tens of particles, and at smaller scales (a few particles across) they consisted of close-packed particle arrangements that formed local, polycrystalline regions separated by grain boundaries. For <5% strain, a few channel cracks appear, mainly at large scale residual deposition defects or occasional multiparticle voids in the film. These are a few micrometers apart and act as nucleation sites for the initial cracks, thus setting the largest crack distance in our experiments. Increasing the strain to 15% adds straight, but short cracks (<3 μm in length) that run perpendicular to the (horizontal) loading direction. As a result, the monolayer becomes divided into fragments with widths ranging from 200 nm to 1 μm. The fragmentation process continues with strains >15%, however, instead of following straight lines, the new cracks form zigzag shapes, as also observed in related experimental systems.[20]

Higher-resolution images indicate that crack edges do not necessarily follow the local lattice orientation of the monolayer (Figure 1f). A representative distribution of the angle α between cracks and loading direction is plotted in the inset to Figure 2 for different strains. For this plot, α was measured from midlines of crack segments that are longer than 100 nm, and therefore averages over any local, particle-scale roughness along a crack edge (see Figure 1g). At low strains (<15%), α has a sharp peak at 90°, as expected. With further strain, more
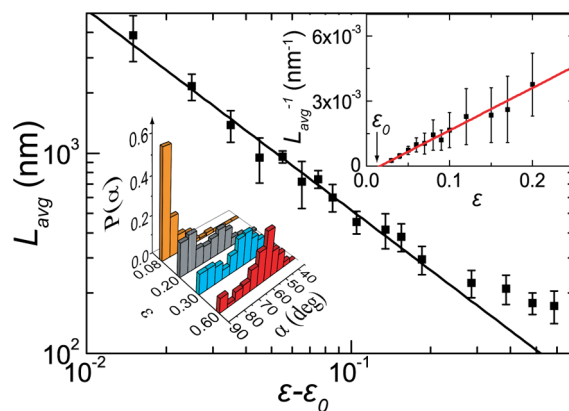

Figure 2. Average crack spacing L_{avg} as function of strain $\varepsilon - \varepsilon_0$ for 5.2 nm diameter Au nanoparticle monolayers. Insets: Determination of strain onset ε_0 (upper right); probability distribution $P(\alpha)$ of crack angle α for different strain ε (lower left).

and more cracks tend to form at $\alpha \approx 60°$ rather than 90°. The crossover between these two different crack regimes takes place between 15 and 20% strain. The fact that cracks no longer remain perpendicular to the stress loading direction can be explained by surface instabilities. From bifurcation analysis,[20,21] the preferred value of α at high strains is related to the hardening exponent N in the stress response, $\sigma = K\varepsilon^N$ and varies from 43° ($N \approx 0$) to 61° ($N = 1$). In our experiments, the second peak in α is centered at 60° ± 1°. This provides evidence that the nanoparticle sheets behave like a linearly elastic material with $N \approx 1$. Interestingly, this linear behavior here holds until fracture, and not only for the small perturbations applied in prior work on freestanding nanoparticle films.[13,16,19]

Another characteristic feature of the SEM images in Figure 1 are bright, narrow strips along the loading direction, indicating local regions of multilayer formation. These are caused by compression perpendicular to the loading direction[22,23] as the PDMS elastomer is stretched (the Poisson ratios of the monolayer and the PDMS substrate are 0.32 ± 0.02[19] and 0.5, respectively). The thickness of these regions, measured by AFM, is approximately twice that of the monolayer, suggesting that under compression, the monolayer fragments did not buckle or fold into the third dimension (as this would lead to thicknesses of 3 particles or more). Instead, it appears that they broke open locally and started to slide over each other like miniature tectonic plates.

The average wavelength λ_{avg} of these horizontal stripe patterns can give a rough estimate of the monolayer's Young modulus via[22] $\bar{E}_f = 3\bar{E}_s[(\lambda_{avg})/(2\pi h_f)]^3$. Here $\bar{E}_f = E_f/(1 - \nu_f^2)$ and $\bar{E}_s = E_s/(1 - \nu_s^2)$ are the plane strain moduli of monolayer film (f) and PDMS substrate (s); ν_f and ν_s are the associated Poisson ratios; h_f is the monolayer thickness. For the 5.2 nm diameter particles, $h_f = 6.9 \pm 0.5$ nm as measured by AFM (which is smaller than adding the Au core diameter (5.2 nm) and the ligand lengths (1.7 nm)[13] on both sides, probably due to compression of ligand layers during the stamping process), and $\lambda_{avg} = 320 \pm 30$ nm. From these the monolayer's Young modulus is found to be $E_f \sim 3.5-6$ GPa, consistent with previous AFM measurements.[13,16]

Analyzing the crack spacing more quantitatively, images were first thresholded and then scanned line by line along the loading direction to identify L_{avg}, the average fragment width or distance between cracks (Figure 2). The onset strain ε_0 for cracking is determined by the intercept $L_{avg}(\varepsilon_0) \to +\infty$, as shown in the inset. The resulting value $\varepsilon_0 \approx 1.6\%$ includes two contributions: any initial prestrain in the sample ε_{pre} and the critical strain for fracture ε_c.[24,25] When mounting the PDMS substrate in the Instron, the substrate's ends are squeezed and the substrate elongates. As a result, the nanoparticle layer attached to the PDMS is under a compressive prestrain, which we estimate as $\varepsilon_{pre} \approx 0.7\%$ from measuring the macroscopic curvature of the slightly bent PDMS substrate. It follows that the onset strain for nanoparticle monolayer fracture ε_c is about 0.9% in our samples.

As shown in Figure 2, we see two regimes for the behavior of L_{avg} versus $\varepsilon - \varepsilon_0$: an inverse scaling of the average fragment width L_{avg} with strain above fracture onset $\varepsilon - \varepsilon_0$ up to about 20%, followed by a weaker dependence at higher strains. In general, the inverse scaling could be preceded by an initial, low-strain regime with wider width distribution and larger L_{avg} due to film heterogeneity.[22,24] The fact that we do not observe this is indicative of the high structural uniformity of our layers at scales >10 particle diameters; local disorder in the particle packing occurs at scales well below the fragment size L_{avg}, which remains >100 nm over the whole range of strains applied. In many other materials and thin metal films, strain localization mechanisms such as local thinning and debonding dominate cracking.[20,26] In our case, given the large ratio of crack spacing to monolayer thickness, the critical strain for debonding is much higher than that for cracking. Thus, the Au monolayer can be assumed to be well bonded to the PDMS substrate,[25] at least up to 15−20% strain.

In this situation, the spatial stress profile in the film can be described by a shear-lag model.[22,27−29] Because of the large mismatch of elastic response between the Au monolayer and the PDMS substrate when stretched, two "shear zones" transfer tensile stress to the layer (see Figure 1a). The length L_s of a shear zone is determined by[22,28] $L_s \approx (2h_f E_f)/E_s$. In our case, $L_s > 10$ μm is much larger than the average fragment width, the tensile stress reaches its maximum at the fragment center, and the fragment tends to crack at its midpoint when the maximum tensile stress exceeds σ^*, the fracture strength of the layer. Each subpiece cracks again when the strain is doubled so that the average fragment width varies with applied strain according to[22]

$$L_{avg} = \frac{2h_f\sigma^*}{E_s(\varepsilon - \varepsilon_0)} \tag{1}$$

This relationship well predicts how the average fragment width changes with applied strain (Figure 2). The one free parameter, the average fracture strength, is determined from a fit, which gives $\sigma^* = 11.0 \pm 2.6$ MPa. This value is similar to cross-linked thin polymer films.[22] Because the nanoparticles in monolayers are only connected by short ligand interdigitation with no cross-linking at all, it is remarkable that their fracture strength is comparable to cross-linked polymer films.

For strains larger than 20%, the plots deviate from the prediction of eq 1. It is likely that at this point the yield strength for interfacial shear is reached and the fragments start to slip on the substrate.[25] The slipping interface makes it harder to crack the fragments further, so the fragmentation rate starts to decrease. Other possibilities might include out-of-plane curling of the nanoparticle layer at large strain;[30,31] however, the E_f/E_s ratio in our experiments would suggest that any vertical deformation of a fragment due to curling is <2 nm and thus contributes negligibly to the applied strain.

The fact that these cracks do not propagate as in brittle films[11,12] can be attributed to ductilily at their crack tips. Indeed, this is the only evidence we find of deviations from linear elastic behavior. It indicates that the material's behavior at the local, few-particle scale can be quite different, and it corroborates what we observed previously[19] with slits cut into freestanding monolayer sheets, namely that the local particle configuration around the tips of the slits can be deformed significantly under stress.[32]

Of course, the fragments do not always break at exactly the midpoint between two existing cracks and there will be a distribution in the fragment widths. On the basis of a weakest link picture for failure, which considers material defects across a wide range of scales,[24] a Weibull distribution is commonly assumed. In our experiments, we have sufficient resolution to determine this distribution directly and do not have to make assumptions (Figure 3a).

The fact that a Gaussian distribution fits well points to the absence of macroscopic defects in our samples and suggests that the relevant disorder occurs over a narrow range of length scales.[33] Such a Gaussian fragment width distribution can arise from an interparticle bond strength distribution of Gaussian form. To investigate this, we analyzed a simple one-dimensional (1D) simulation consisting of a chain of particles with fracture strength between neighbors picked from a Gaussian with mean σ^* and standard deviation $\Delta\sigma$. The chain is then fragmented by applying the shear-lag model M times in succession, and the final fragment widths are analyzed as a function of M. Figure 3b shows the results using a fixed value of 3.6 MPa chosen to produce the overall best fit to all experimental data (further simulation results show that deviations from a Gaussian shape, observed in tails of the experimental crack spacing distribution data, might come from the 2D geometry of cracks, both length
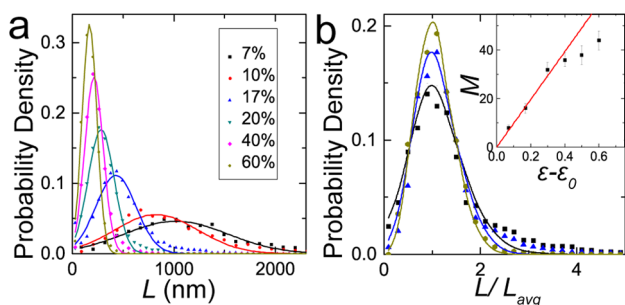
Figure 3. (a) Crack spacing distribution for different strains as indicated. Symbols, experimental data; lines, Gaussian fits. (b) Normalized crack spacing distribution. Symbols, experimental data; lines, simulation as described in text. Strain levels are indicated by the same symbols and colors as in (a). Inset: Fitting parameter M for different strains.

and orientation, which is not considered in the 1D model). The simulations used an initial chain length of 2000 particles and the data shown are ensemble averaged over 10^4 independent trials. With increasing strain and therefore larger number M of fragments, the distribution is found to become narrower, as in the experiments. Furthermore, the variable M is seen to be proportional to the experimental strain, at least up to the point that slipping is reached. The considerable width of the fracture strength distribution in the experiments, almost one-third of its mean, can be understood as arising from a combination of factors that all can affect the bond strength, besides local lattice defects also including variations in interparticle spacing or in the ligand coverage of individual particles.

The monolayer strength is a result of the interdigitation of ligands from neighboring particles. The degree of this interdigitation will depend on the curvature of particles, and thereby the particle size.[13] This suggests that increasing the particle size should increase fracture strength. This is indeed what we find when switching to larger Au cores (9.1 nm diameter) with the same capping ligands (Figure 1g). The resulting ~10 nm thick monolayers were found to have a fracture strength of 15.2 ± 1.7 MPa (Figure 4), roughly 40% higher than that of the ~6.9 nm thick monolayers.

Building up thicker films, a monolayer at a time, our experiments can directly investigate how film thickness affects
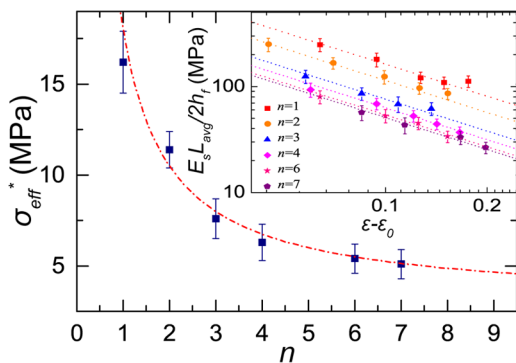

Figure 4. Dependence of effective fracture strength σ_{eff}^* on film thickness, parametrized by number of monolayers n, for 9.1 nm diameter Au nanoparticles. Inset: Normalized average crack spacing $E_s L_{avg}/2h_f$ as function of strain for different n, with dashed lines indicating power law with exponent −1 (eq 1). The vertical position of the lines in this log−log plot gives the effective fracture strength.

fracture. In partially overlaid monolayers on the same substrate, where they are subjected to the same applied strain, differences are immediately noticeable when comparing regions on either side of a step-edge. As shown in Figure 1h, the crack spacing in the bilayer region is clearly larger than in the monolayer, and cracks tend to stop at the step-edge. Analyzing the average crack spacing L_{avg} for films $n = 1$ to 7 layers thick (Figure 4 inset), we find that eq 1 remains valid but with an effective fracture strength σ_{eff}^* that decreases with increasing n before eventually saturating. Similar behavior is observed in thin metal coatings that have been grown on substrates,[23] where it is typically attributed to larger initial defect sizes in thicker films. However, our system is deposited "layer-by-layer", and the initial defect sizes are not expected to change with the number of layers. Instead, we believe this behavior is indicative of inhomogeneity in stress across the thickness.[34] Because all layers were prepared the same and from the same set of nanoparticles, it is unlikely they varied significantly in inherent strength. However, the first monolayer is deposited on the PDMS substrate and thus likely to exhibit different prestress compared to the subsequent layers. The fact that the effective fracture strength decreases implies that, at fracture, the $2^{nd}-n^{th}$ layers have taken up proportionally less stress than the first layer; for example, they started out at some residual stress level that was lower than that of the first layer. Once the stress in the first layer exceeds σ^*, the fracture will propagate across the full film thickness $h_f = nh_0$, where h_0 is an individual layer thickness. This point defines σ_{eff}^* for the n-layer system. If we assume the simplest case, where the residual stress in the first layer is larger by a fixed amount $\Delta\sigma_r$, we have $\sigma_{eff}^* = [\sigma^* h_0 + (n-1)(\sigma^* - \Delta\sigma_r)h_0]/nh_0) = \sigma^* - \Delta\sigma_r + (\Delta\sigma_r/h)$. This matches the data very well with $\Delta\sigma_r = 0.8\sigma^* \approx 12$ MPa (Figure 4 red dashed line), implying a residual strain difference $\Delta\varepsilon_r = (\Delta\sigma_r/E_f) \approx 0.3\%$.

In summary, we investigated microcrack patterns in self-assembled close-packed Au nanoparticle layers. From the fragment width distribution, we extracted the intrinsic fracture strength and its distribution and related it to the interparticle bond strength. Relative to their thickness, monolayers were found to be significantly stronger than multilayers, an effect that we tracked here in detail for the first time and attributed to differences in residual strain during deposition.

■ AUTHOR INFORMATION

Corresponding Author
*E-mail: yifanw@uchicago.edu.

Notes
The authors declare no competing financial interest.

■ ACKNOWLEDGMENTS

■ REFERENCES

(1) Shipway, A. N.; Katz, E.; Willner, I. *ChemPhysChem* **2000**, *1*, 18.

(2) Sun, S. H.; Murray, C. B.; Weller, D.; Folks, L.; Moser, A. *Science* **2000**, *287*, 1989.

(3) Trindade, T.; O'Brien, P.; Pickett, N. L. *Chem. Mater.* **2001**, *13*, 3843.

(4) Min, Y.; Akbulut, M.; Kristiansen, K.; Golan, Y.; Israelachvili, J. *Nat. Mater.* **2008**, *7*, 527.

(5) Talapin, D. V.; Lee, J. S.; Kovalenko, M. V.; Shevchenko, E. V. *Chem. Rev.* **2010**, *110*, 389.

(6) Nie, Z.; Petukhova, A.; Kumacheva, E. *Nat. Nanotechnol.* **2010**, *5*, 15.

(7) Shevchenko, E. V.; Talapin, D. V.; Kotov, N. A.; O'Brien, S.; Murray, C. B. *Nature* **2006**, *439*, 55−59.

(8) Griffith, A. A. *Philos. Trans. R. Soc. London, Ser. A* **1921**, *221*, 163.

(9) Thomson, R. M. *J. Phys. Chem. Solids* **1987**, *48*, 965−983.

(10) Hutchinson, J. W.; Suo, Z. *Adv. Appl. Mech.* **1992**, *29*, 63.

(11) Fineberg, J.; Marder, M. *Phys. Rep.* **1999**, *313*, 1−108.

(12) Bouchbinder, E.; Fineberg, J.; Marder, M. *Annu. Rev. Condens. Matter Phys.* **2010**, *1*, 371−395.

(13) He, J.; Kanjanaboos, P.; Frazer, N. L.; Weis, A.; Lin, X. M.; Jaeger, H. M. *Small* **2010**, *6*, 1449−1456.

(14) Lin, X. M.; Jaeger, H. M.; Sorensen, C. M.; Klabunde, K. J. *J. Phys. Chem. B* **2001**, *105*, 3353−3357.

(15) Liao, J. H.; Bernard, L.; Langer, M.; Schönenberger, C.; Calame, M. *Adv. Mater.* **2006**, *18*, 2444.

(16) Mueggenburg, K. E.; Lin, X. M.; Goldsmith, R. H.; Jaeger, H. M. *Nat. Mater.* **2007**, *6*, 656−660.

(17) He, J.; Lin, X. M.; Chan, H.; Vukovic, L.; Kral, P.; Jaeger, H. M. *Nano Lett.* **2011**, *11*, 2430−2435.

(18) Eah, S. K. *J. Mater. Chem.* **2011**, *21*, 16866−16868.

(19) Kanjanaboos, P.; Joshi-Imre, A.; Lin, X. M.; Jaeger, H. M. *Nano Lett.* **2011**, *11*, 2567−2571.

(20) Xiang, Y.; Li, T.; Suo, Z. G.; Vlassak, J. J. *Appl. Phys. Lett.* **2005**, *87*, 161910.

(21) Hutchinson, J. W.; Tvergaard, V. *Int. J. Mech. Sci.* **1980**, *22*, 339−354.

(22) Chung, J. Y.; Lee, J. H.; Beers, K. L.; Stafford, C. M. *Nano Lett.* **2011**, *11*, 3361−3365.

(23) Cordill, M. J.; Taylor, A.; Schalko, J.; Dehm, G. *Metall. Mater. Trans. A* **2010**, *41A*, 870.

(24) Heinrich, M.; Gruber, P.; Orso, S.; Handge, U. A.; Spolenak, R. *Nano Lett.* **2006**, *6*, 2026−2030.

(25) Sun, J. Y.; Lu, N. S.; Yoon, J.; Oh, K. H.; Suo, Z. G.; Vlassak, J. J. *J. Appl. Phys.* **2012**, *111*, 013517.

(26) Stören, S.; Rice, J. R. *J. Mech. Phys. Solids* **1975**, *23*, 421−441.

(27) Handge, U. A. *J. Mater. Sci.* **2002**, *37*, 4775−4782.

(28) Bazhenov, S. L.; Volynskii, A. L.; Alexandrov, V. M.; Bakeev, N. F. *J. Polym. Sci., Part B* **2002**, *40*, 10−18.

(29) Begley, M. R.; Bart-Smith, H. *Int. J. Solids Struct.* **2005**, *42*, 5259−5273.

(30) Douville, N. J.; Li, Z.; Takayama, S.; Thouless, M. D. *Soft Matter* **2011**, *7*, 6493.

(31) Taylor, A. A.; Cordill, M. J.; Dehm, G. *Philos. Mag.* **2012**, *92*, 3363.

(32) Ritchie, R. O. *Int. J. Fract.* **1999**, *100*, 55.

(33) Lu, C.; Danzer, R.; Fischer, F. D. *Phys. Rev. E* **2002**, *65*, 067102.

(34) Volynskii, A. L.; Panchuk, D. A.; Yarysheva, L. M.; Bazhenov, S. L.; Bakeev, N. F. *Dokl. Phys. Chem.* **2008**, *422*, 249.